Homogenization of helical beam-like structures: application to single-walled carbon nanotubes

Tanguy Messager, Patrice Cartraud

Homogenization of helical beam-like structures: application to single-walled carbon nanotubes

Tanguy Messager · Patrice Cartraud

T. Messager (✉)
Université de Nantes, Nantes Atlantique Universités,
Nantes, France
e-mail: tanguy.messager@univ-nantes.fr

T. Messager · P. Cartraud
Institut de Recherche en Génie civil et Mécanique (GeM),
UMR CNRS 6183 Ecole Centrale de Nantes,
BP 92101, 44321 Nantes cédex3, France
e-mail: patrice.cartraud@ec-nantes.fr

Abstract This work is devoted to the computation of axial stiffness of helical beam-like structures. Starting from the homogenization theory of periodic slender domains and taking benefit of the property of helical symmetry, the overall elastic behavior can be obtained from the solution of three-dimensional problems posed on a reduced basic cell. The mechanical analysis of this reduced basic cell performed using a concise FE model allows therefore to compute easily the anisotropic beam homogenized stiffness coefficients. The accuracy and usefulness of this approach is demonstrated by comparisons with reference solutions and large FE model results for two numerical volume structure examples: a wire spring and a stranded "6 + 1" rope. The homogenization procedure is then applied to single-walled carbon nanotubes and it is shown from the two helical symmetries that their basic cell can be reduced to three beam elements.

Keywords Homogenization · Effective properties · Helical symmetry · FEM · Nanotube

1 Introduction

The various applications of homogenization discussed in the literature have demonstrated its efficiency and usefulness for the overall modeling of beam-like structures exhibiting periodic geometrical or material heterogeneity as detailed in [3–5,12–14]. This approach is based on the asymptotic expansion method, and gives the first-order approximation of the three-dimensional heterogeneous solution from the solution of two successive problems: a microscopic three-dimensional problem, posed on the axial period of the structure (the basic cell), and, a macroscopic one-dimensional problem. The macroscopic problem equations show that the overall behavior is that of a Navier–Bernoulli–Saint Venant beam. Its effective elastic properties are obtained from the solution of the microscopic problem, which is usually computed from the finite element (FE) analysis of the structure axial period.

In a previous work [4], this computational homogenization method was presented for beam-like structures with axial periodicity, i.e. structures formed by periodic repetition of a basic cell in the slenderness direction. In the case of helical structures, this latter approach can also be applied since any helical structure exhibits axial periodic heterogeneity, the length of the period being defined as the pitch of the helix. However, for such helical structures subjected to axial loadings, taking advantage of the helical symmetry enables the definition of a reduced basic cell, therefore allowing significant reduction of the size of the numerical model. The numerical solution of this microscopic problem is achieved using multi-point displacement constraints expressed in local cylindrical axes between the opposite nodes of a concise FE model of this reduced basic cell. These relationships then act as kinematic boundary conditions for the reduced basic cell problem.

In this paper, the homogenization procedure is applied to compute the elastic axial stiffness of two helical volume structures: a wire spring and a stranded "6 + 1" stranded rope. For such structures, it is shown that taking benefit of the helical symmetry, the microscopic problem can be posed on a basic cell of arbitrary length. Therefore, this length is chosen

to be small and the effective properties are computed using elementary solid FE models, comprising only one layer of elements in the helix direction. The accuracy of the results is assessed with respect to analytical solutions, and to reference numerical solutions obtained from the FE analysis of a domain composed with a large number of axial periods. Next, the developed approach is used for the computation of the overall axial behavior of single-walled carbon nanotubes (SWCNTs). These nanotubes are assumed to behave as space-frame structures and are modeled using straight 3D beam FE representing the atomic bonds. Considering the two helical symmetries of such nanostructures, the basic cell can be reduced to only one half of a hexagon, and modeled using three beam FE. The homogenized results show very good agreement with reference numerical results. The procedure is then applied for zigzag and armchair SWCNTs, providing the evolution of the tensile and torsion overall stiffness as a function of their geometrical parameters.

2 The homogenization procedure

The summation convention on repeated indices will be used in the next sections. Dots and semi-colons denote the scalar and double products of tensors, e.g.: $\sigma.n = \sigma_{ij}n_j$ and $a : e = a_{ijkl}e_{kl}$ respectively.

2.1 Axial periodicity and helical symmetry

The purpose of the homogenization theory, based on the asymptotic expansion method, is to substitute the actual three-dimensional heterogeneous and slender domain with a homogeneous anisotropic beam. A previous study based on this approach has been successfully applied for the computation of beams with axial periodic microstructure [4]. For the present work, let us consider a lengthy helical structure of constant period length L with a homogeneous constant cross-section as depicted in Fig. 1a.

The objective is to obtain the overall elastic axial behavior of such beam-like structure by relating the extension and torsion macroscopic strains E^E and E^T to the tensile force N and the axial torque M schematized in Fig. 2.

The lengthy structures under consideration are assumed to exhibit no coupling between bending and other loadings such as tension and torsion. The geometry is characterized by two small parameters:

- e: the slenderness, i.e. the ratio of the width of the cross-section to the total length of the structure;
- ε: the ratio of the length of the period to the total length of the structure.

Following the discussion and conclusions detailed in [3,12,14], these two parameters are assumed to tend to zero simultaneously: it thus allows the use of the asymptotic expansion method with one small parameter. The starting point of this method is the formulation of the three-dimensional heterogeneous problem. Its displacement solution is searched under the form:

$$u(x) = u^0_\alpha(x_3)e_\alpha + \varepsilon u^1(x_3, y_1, y_2, y_3) + \varepsilon^2 u^2(x_3, y_1, y_2, y_3) + \cdots \quad (1)$$

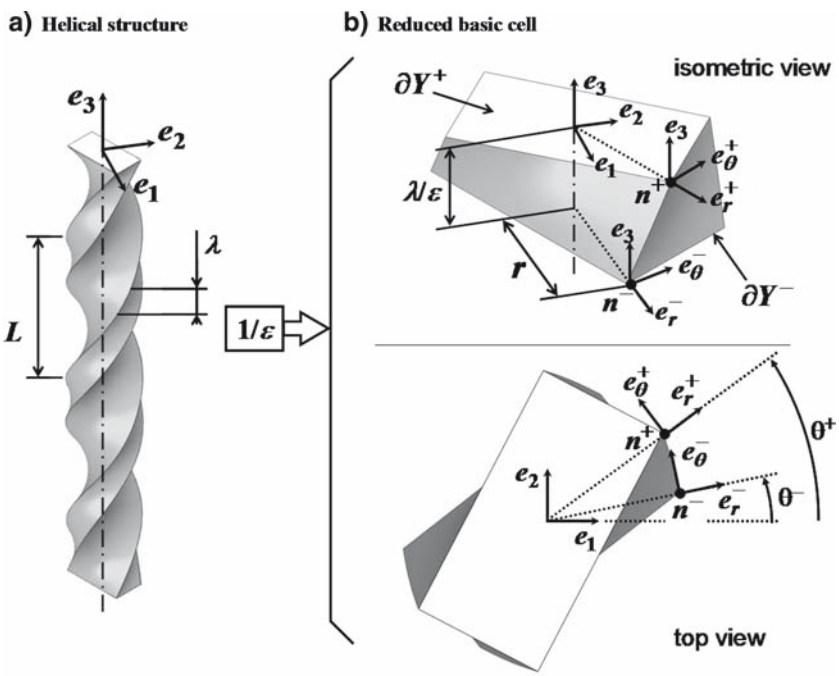

Fig. 1 Periodic helical structure and its reduced basic cell

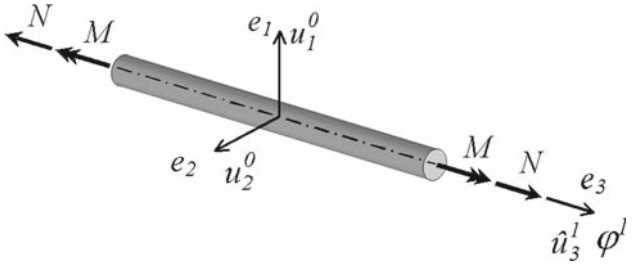

Fig. 2 Displacements and axial loading of a e_3-axis beam-like structure

where α indicates the out of axis directions (i.e. $\alpha = 1, 2$). The macroscopic coordinates x_i of the problem are related to the global axis system $(e_1; e_2; e_3)$ represented in Fig. 1a, the microscopic ones being defined as follows:

$$y_i = x_i/\varepsilon \tag{2}$$

In the case of axial loading, and under the assumption that there are no coupling between bending and tension or torsion, the bending deflection u_α^0 (with $\alpha = 1, 2$) of Eq. (1) vanishes. If the structure is considered as a medium with axial periodic microstructure, the kth order displacement u^k fulfills the following property:

$$u^k(x_3, y_1, y_2, y_3) = u^k\left(x_3, y_1, y_2, y_3 + \frac{L}{\varepsilon}\right) \tag{3}$$

This property leads to a microscopic problem posed on a basic cell of length L/ε.

However, taking into account the helical symmetry enables setting a microscopic problem posed on a fraction of the previous basic cell as illustrated in Fig. 1b. We denote n^- and n^+ two opposite points situated in the ∂Y^- and ∂Y^+ sides of this slice of axial length λ/ε of the structure and both placed at a radius r measured with respect to the helical axis e_3. The two cylindrical local coordinate systems $\left(e_r^-; e_\theta^-; e_3^-\right)$ and $\left(e_r^+; e_\theta^+; e_3^+\right)$ depicted in Fig. 1b are connected to these points and the radial inclinations (measured with respect to the structural axis e_1) are denoted by θ^- and θ^+, respectively.

Such structure subjected to axial loading satisfies the property of translation-rotation helical symmetry [16,20]. Therefore, in the same way that Eq. (3) expressed the structure axial periodicity, a new relation will be used for helical symmetry. In this case, the displacement components of two points n^- and n^+ situated on the same helicoidal line, expressed in the associated helical system, are identical. The helical symmetry can thus be written in the related local cylindrical coordinate systems (see Fig. 1b) as follows:

$$u^k\left(r, \theta^-, y_3\right) \cdot e_i^- = u^k\left(r, \theta^+, y_3 + \frac{\lambda}{\varepsilon}\right) \cdot e_i^+ \tag{4}$$

with $k \geqslant 1$ and where $y = (r, \theta, y_3)$ is the microscopic variable set and $i = r, \theta, 3$. The difference between the two angular + and − locations can be easily related to the fraction λ:

$$\theta^+ - \theta^- = 2\pi L/\lambda \tag{5}$$

thus providing:

$$u^k\left(r, \theta^-, y_3\right) \cdot e_i^- = u^k\left(r, \theta^- + \frac{2\pi L}{\lambda}, y_3 + \frac{\lambda}{\varepsilon}\right) \cdot e_i^+ \tag{6}$$

This helical symmetry property plays the role of boundary conditions and therefore enables posing the microscopic problem on a concise length λ/ε instead of using the basic cell of length L/ε when only the axial periodicity is taken into account. The helical symmetry hence allows the development of an efficient homogenization procedure for the computation of helical beam-like structures as detailed in the following.

It could be noticed that the helical symmetry property of the displacements field expressed in local coordinates has also been employed in [21] for eigenanalysis but in a different framework than the asymptotic expansion method.

2.2 Reduced basic cell problem

Applying the classical approach of homogenization theory, the elastic response of the actual three-dimensional heterogeneous and slender domain can be obtained from the successive solving of two mechanical problems:

- a microscopic elastic problem posed on a three-dimensional basic cell corresponding to one slice of the structure (of length λ/ε);
- a macroscopic one-dimensional problem of an homogeneous and anisotropic e_3-axis beam subjected to a tensile force N and an axial torque M (see Fig. 2) with associated extension and torsion macroscopic strains E^E and E^T.

As shown in [4], the macroscopic strain components of extension and torsion are given by:

$$\begin{cases} E^E(x_3) = \partial \hat{u}_3^1/\partial x_3 \\ E^T(x_3) = \partial \varphi^1/\partial x_3 \end{cases} \tag{7}$$

where $\hat{u}_3^1$ and φ^1 are the macroscopic axial displacement and rotation (see Fig. 2) which appears in the solution of the -1th order microscopic elastic problem.

Denoting div_y the divergence operator with respect to the microscopic variables y, the basic cell problem is given by:

$$\begin{cases} \mathrm{div}_y \sigma = 0 \\ \sigma = a{:}e \\ \sigma.n = 0 \quad \text{on } \partial Y_\ell \\ u^{hel} \text{`hel'} \quad \text{and} \quad \sigma.n \text{`anti-hel'} \end{cases} \tag{8}$$

where σ and a are the microscopic stress and the elastic moduli tensors respectively and ∂Y_ℓ stands for the lateral surface of the basic cell. Besides, the superscript ' *hel*' denotes the helical symmetry property (see Eq. (6)) and 'anti-hel' means that the values of $\sigma.n$ are opposite for the two points n^- and n^+ on the sides ∂Y^+ and ∂Y^- shown in Fig. 1b. The related strain components are given by:

$$\begin{cases} e_{rr} = e_{y_{rr}}\left(u^{hel}\right) \\ e_{r\theta} = e_{y_{r\theta}}\left(u^{hel}\right) \\ e_{r3} = e_{y_{r3}}\left(u^{hel}\right) \\ e_{\theta\theta} = e_{y_{\theta\theta}}\left(u^{hel}\right) \\ e_{\theta 3} = e_{y_{\theta 3}}\left(u^{hel}\right) + rE^T/2 \\ e_{33} = e_{y_{33}}\left(u^{hel}\right) + E^E \end{cases} \tag{9}$$

e_y being the strain operator in microscopic variable y.

Due to the linearity of Eqs. (7–9), the helical displacement and microscopic stress fields can be additively decomposed in a tensile and torsion related components as follows:

$$\begin{cases} u^{hel} = \chi^{\mathbf{E}}(y)E^E(x_3) + \chi^T(y)E^T(x_3) \\ \sigma = \sigma^{\mathbf{E}}(y)E^E(x_3) + \sigma^T(y)E^T(x_3) \end{cases} \tag{10}$$

The stress solution of the microscopic problem is a function of the macroscopic strains E^E and E^T. Integrating over the cross-section and averaging with respect to the scaled length λ/ε of the basic cell domain denoted Y, the macroscopic axial force N and the torque M depicted in Fig. 2 are then given by:

$$\begin{cases} N = N(x_3) = \dfrac{\varepsilon}{\lambda}\displaystyle\int_Y \sigma_{33} r\, dr\, d\theta\, dy_3 \\ M = M(x_3) = \dfrac{\varepsilon}{\lambda}\displaystyle\int_Y \sigma_{\theta 3} r^2\, dr\, d\theta\, dy_3 \end{cases} \tag{11}$$

It then allows obtaining the overall axial elastic behavior expressed in the following matrix form:

$$\begin{Bmatrix} N \\ M \end{Bmatrix} = \left[a^{hom}\right] \begin{Bmatrix} E^E \\ E^T \end{Bmatrix} = \begin{bmatrix} a^{hom}_{EE} & a^{hom}_{ET} \\ a^{hom}_{TE} & a^{hom}_{TT} \end{bmatrix} \begin{Bmatrix} E^E \\ E^T \end{Bmatrix} \tag{12}$$

where a^{hom}_{EE} and a^{hom}_{TT} are the homogenized stiffness coefficients of tension and torsion, respectively. Moreover, it should be underlined that the two coupling terms satisfy the matrix symmetry condition, see [3]:

$$a^{hom}_{ET} = a^{hom}_{TE} \tag{13}$$

In that way, the microscopic mechanical analysis provides the beam's overall stiffness coefficients of $\left[a^{hom}\right]$.

From Eq. (10), a microscopic field u can be defined from the previous helical displacement solution u^{hel} as follows:

$$\begin{cases} u_r = u^{hel}_r \\ u_\theta = u^{hel}_\theta + r y_3 E^T \\ u_3 = u^{hel}_3 + y_3 E^E \end{cases} \tag{14}$$

Considering the helical symmetry of u^{hel} expressed by Eq. (6), the displacement solution u of the reduced basic cell problem is not dependent of the value of λ.

2.3 Numerical implementation

The numerical solving of the basic cell problem for beam-like structures with axial periodicity is presented in [4]. The same type of approach is used herein, namely the use of multi-point displacement constraints. In the case of helical symmetry, such relations are expressed in local cylindrical axes, as shown in the following.

The solution of the reduced basic cell problem consists in the computation of the displacement u defined in Eq. (14). It can be carried out using a three-dimensional FE model. We denote U_i^- and U_i^+ the displacement degrees of freedom (DOFs) expressed in the local cylindrical frames $\left(e_r^-; e_\theta^-; e_3^-\right)$ and $\left(e_r^+; e_\theta^+; e_3^+\right)$ of two opposite nodes n^- and n^+ of the FE model, see Fig. 1b. Taking into account the helical symmetry expressed by Eq. (6), Eq. (14) leads to a set of linear relationships which can be written as:

$$\begin{cases} U_r^+ - U_r^- = 0 \\ U_\theta^+ - U_\theta^- = r\lambda E^T/\varepsilon \\ U_3^+ - U_3^- = \lambda E^E/\varepsilon \end{cases} \tag{15}$$

It should be underlined that the rigorous homogenization approach used in this paper enables the study of an arbitrary basic cell without any assumption, by contrast with the work presented in [10,11], where kinematic assumptions are used on the opposite sections of the concise slice FE models.

The numerical computations are performed by applying linear multi-point displacement constraints, given by Eq. (15), between each pair of opposite nodes of the FE model discretizing the reduced basic cell. Following Eq. (12), the

strain energy of the basic cell is found to be:

$$\Pi = \frac{1}{2}\int_{\lambda/\varepsilon} \sigma : e \, dy = \frac{\lambda}{2\varepsilon} \left\{ \begin{matrix} N \\ M \end{matrix} \right\}^T \left\{ \begin{matrix} E^E \\ E^T \end{matrix} \right\}$$
$$= \frac{\lambda}{2\varepsilon} \left\{ \begin{matrix} E^E \\ E^T \end{matrix} \right\}^T \left[a^{hom}\right] \left\{ \begin{matrix} E^E \\ E^T \end{matrix} \right\} \quad (16)$$

The values of the $\left[a^{hom}\right]$ stiffness matrix components can subsequently be deduced from three successive FE computations:

- $a_{EE}^{hom} = 2\Pi\varepsilon/\lambda$ applying $E^E = 1$ and $E^T = 0$
- $a_{TT}^{hom} = 2\Pi\varepsilon/\lambda$ applying $E^E = 0$ and $E^T = 1$
- $a_{ET}^{hom} = a_{TE}^{hom} = \frac{\Pi\varepsilon}{\lambda} - \frac{a_{EE}^{hom} + a_{TT}^{hom}}{2}$ applying $E^E = 1$ and $E^T = 1$.

3 Numerical examples

3.1 Volume FE models

As can be seen, Eq. (6), which expresses the helical symmetry property, is independent of λ. Therefore, any value of λ can be considered to obtain the basic cell solution, and only one layer of three-dimensional elements is needed to compute the overall elastic axial stiffness. This homogenization methodology consequently enables the use of concise FE volume models leading to reduced computation time.

The homogenization approach developed has been first applied for the computations of the homogenized stiffness matrix $\left[a^{hom}\right]$ of a wire spring and a stranded "6+1" rope both shown in Fig. 3a and b, respectively. The homogenization procedure has been therefore coupled with FE slice models of the structures. The numerical axial stiffness values obtained are compared thereafter with analytical reference solutions and with those calculated using FE models of large lengths obtained from the helical translation-rotation of the reduced basic cell meshes.

3.1.1 Helical wire spring

The geometry of wire springs of constant spiral angle, widely used in mechanical systems [7,11], is characterized by the coil radius R and the helical angle α measured with respect to the mean-line of the wire as depicted in Fig. 3a. The corresponding axial period length (or pitch) is then related to these parameters by:

$$L = 2\pi R/\tan\alpha \quad (17)$$

The numerical investigations detailed subsequently used the following values: $R = 20\,\text{mm}$; $\alpha = 80°$. As illustrated in Fig. 3a, the wire studied is considered to have a circular constant section with radius $R_W = 5\,\text{mm}$. The constitutive material's Young modulus and Poisson's ratio have been chosen to be $E = 200$ GPa and $\nu = 0.3$, respectively.

Most often in analytical approaches, the wire is considered as a beam subjected to only shear and torque, the effect of the helical angle being taken into account using correction factors [11]. A curved beam analytical modeling of coiled springs is proposed in [7]: this approach, used as a reference for the present study, leads to the following closed-form expressions for the tensile and torsion stiffness terms a_{EE}^{hom} and a_{TT}^{hom} of a wire spring with circular cross-section (the coupling terms a_{ET}^{hom} and a_{TE}^{hom} being not studied herein):

$$\begin{cases} a_{EE}^{hom} = \pi E R_W^4/4(1+\nu)R^2\tan\alpha \\ a_{TT}^{hom} = \pi E R_W^4/4\tan\alpha \end{cases} \quad (18)$$

The corresponding values for the studied numerical example are reported in Table 1.

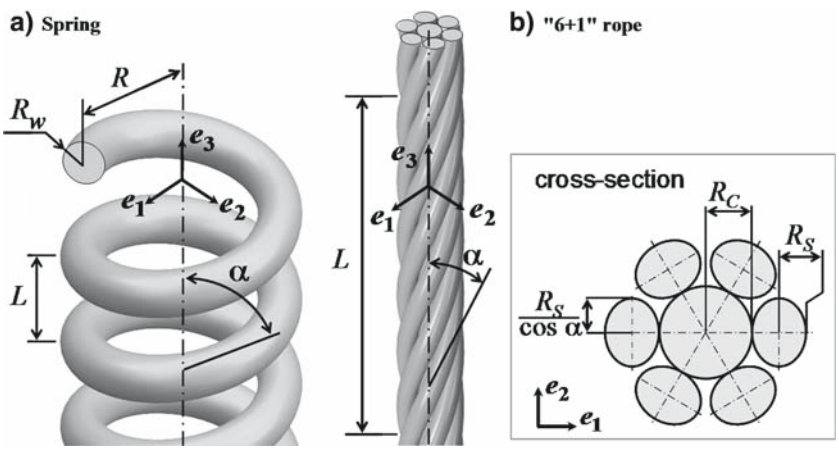

Fig. 3 Geometries of the helical volume structures studied

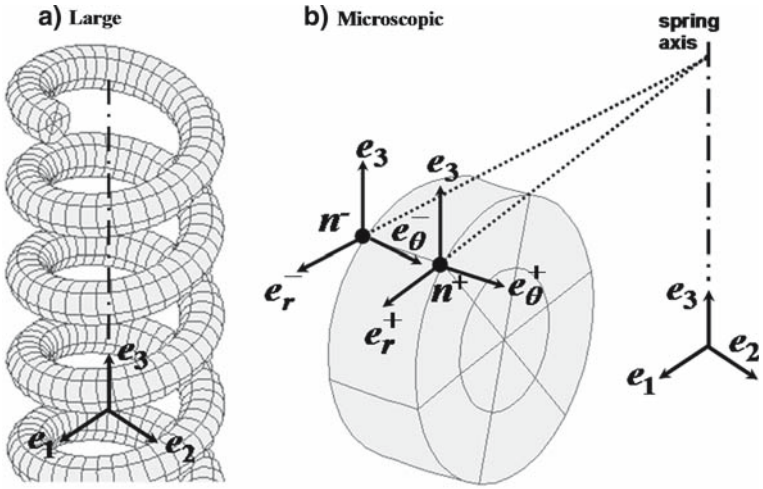

Fig. 4 FE models of the helical spring

Table 1 Stiffness coefficients of the helical wire spring

Model	a_{EE}^{hom} (10^3 N)	a_{TT}^{hom} (N m^2)	CPU time (s)
Analytical	33.29	17.31	
Large FE	33.50	17.01	10.2
Microscopic FE	33.23	16.99	0.3

Two three-dimensional FE models of the coiled spring have been computed using Samcef commercial software. First, a large model is presented in Fig. 4a: the exact geometry is generated by extruding a circular surface along the centroidal helical curve of the wire. As can be seen in Fig. 4a, the wire section is discretized using six 12-node and six 16-node bricks. The computation of the overall behavior is achieved following a classical approach: as detailed in [8], the effective properties are calculated using four successive combinations of the axial loads (applying tension N or torsion M) and the boundary conditions (the axial displacement and rotation being free or locked) applied on rigid body elements linked to the end sections of the spring. For a given loading case, the overall strains are computed from the axial displacement and rotation values at the center of the end cross-sections. Therefore, these four elastic linear analyses provide the stiffness coefficients, and the symmetry property expressed by Eq. (13) can then be checked. In that way, preliminary tests have shown that six axial periods have to be modeled in order to limit the influence of the end effects. This large FE model thus consists of 2880 quadratic solid FE.

The second FE model has been coupled to the homogenization procedure. As noticed previously, the microscopic model corresponds to one slice of the previous large FE model as depicted in Fig. 4b: only 12 solid FE are therefore used, the reduced basic cell's length being $\lambda = L/40$ for this example. The linear displacement relations for the displacement DOFs defined by Eq. (15), expressed in the local cylindrical frames, have been prescribed for each couple of opposite nodes n^- and n^+ as those schematized in Fig. 4b.

The overall stiffness terms obtained using these two FE computations are detailed in Table 1. The CPU computation times of one stiffness coefficient on a standard workstation are also reported. As can be seen, the microscopic FE model provides accurate results and enables significant reduction of the CPU time.

3.1.2 "6 + 1" stranded cable

Stranded ropes are commonly used for many engineering applications such as bridges, mooring lines or pre-stressed structures [6,8,15,17]. These beam-like structures are mainly constituted of wires wrapped together or around a central straight core, thus exhibiting helical symmetry. Besides, the end anchorages generally employed for such cables allow radial pivoting, therefore leading only axial macroscopic loading components [8,15].

The present work is focused on a "6 + 1" cable geometry: as depicted in Fig. 3b, six helical strands having circular cross-sections are wrapped around a cylindrical core following a constant helical angle α (measured between the mean-line of the strands and the axial direction e_3). The radius of the strands and the core being denoted by R_S and R_C respectively, the axial period length L is given by:

$$L = 2\pi (R_C + R_S)/\tan\alpha \tag{19}$$

The homogenization procedure proposed in this paper has been applied using the numerical values of the example detailed in [15]: the cable geometry is characterized by $R_C = 2.675$mm, $R_S = 2.59$mm and $\alpha = 8.18°$. The Young's modulus and Poisson's ratio of the constitutive material of

the core and the strands are $E = 200\text{GPa}$ and $\nu = 0.3$, respectively.

Several authors have developed analytical models for predicting the elastic response of spiral cables. A review of the different approaches is available in [8]: the model developed by Labrosse [15] has been chosen as a reference for the present study. The wire mechanical behavior is described as Love's curved beams and leads to the following closed-form expressions for the stiffness terms:

$$\begin{cases} a_{EE}^{hom} = \pi E \left(R_C^2 + 6 R_S^2 \cos^3\alpha \right) \\ a_{TT}^{hom} = \pi E \left[\dfrac{1}{4(1+\nu)} \left(R_C^4 + 6 R_S^4 \cos^5\alpha \right) \right. \\ \qquad + 6 \cos\alpha \sin^2\alpha R_S^2 \left((R_C + R_S)^2 \right. \\ \qquad \left. \left. + \dfrac{R_S^2}{4} \left(1 + \cos^2\alpha \right) \right) \right] \\ a_{ET}^{hom} = a_{TE}^{hom} = 6\pi E R_S^2 (R_C + R_S) \cos^2\alpha \sin\alpha \end{cases} \quad (20)$$

Table 2 details the values obtained for the numerical example under consideration.

A large FE model of the rope depicted in Fig. 5a has been computed using Samcef. As completed for the coiled spring studied in the previous section, the exact geometry of the cable has been obtained by extruding circular surfaces along each wire mean-line, geometrical approximations having a great influence on results as shown in [19]. Each wire section is meshed using 12 quadratic solid FE similarly to the wire spring. As mentioned in previous works [15,17], the overall elastic axial behavior of such rope appears to be not sensitive to inter-wire contact conditions (rolling and sliding) between the strands and the central core. Therefore, the nodes situated on the external surface of the core have been merged to those of the strands using common nodes [8]. For this large model, the tensile, torsion and coupling stiffness terms are obtained in a similar fashion as for the studied coiled spring using four static linear analysis combining different boundary conditions applied on rigid body elements linked to the end sections. In the same way, preliminary tests have shown that the modeling of three pitch lengths is necessary in order that the overall behavior becomes insensitive to end-effects [8]. This large model hence comprises a total of 5,160 FE.

Taking benefit of the independence of Eq. (6) with respect to λ as done previously for the computation of a spring, the FE model (depicted in Fig. 5b) coupled to the homogenization procedure corresponds to a helical layer of the large model. It hence leads to a fraction value $\lambda = L/86$.

The stiffness coefficient values (and the corresponding CPU time of calculus for one stiffness computation) obtained using the two numerical models are detailed in Table 2. The same example was treated in [4] but considering axial periodicity, which leads to a basic cell corresponding to one cable pitch. It can be checked that the results obtained from the reduced basic cell problem are exactly the same as those available in [4] (see Table 2 of that paper, where there is a misprint in the order of magnitude for the coupling coefficient a_{ET}^{hom}). As in the case of the helical wire spring, the homogenized stiffness obtained from the reduced basic cell problems is in a very good agreement with the analytical model and reference values computed from the large FE model.

Table 2 Stiffness coefficients of the stranded "6 + 1" cable

Model	a_{EE}^{hom} (10^6 N)	a_{TT}^{hom} (N m^2)	a_{ET}^{hom} (10^3 N m)	CPU time (s)
Analytical	29.02	52.91	18.56	
Large FE	28.60	53.82	18.25	405
Microscopic FE	28.63	53.49	18.24	1.2

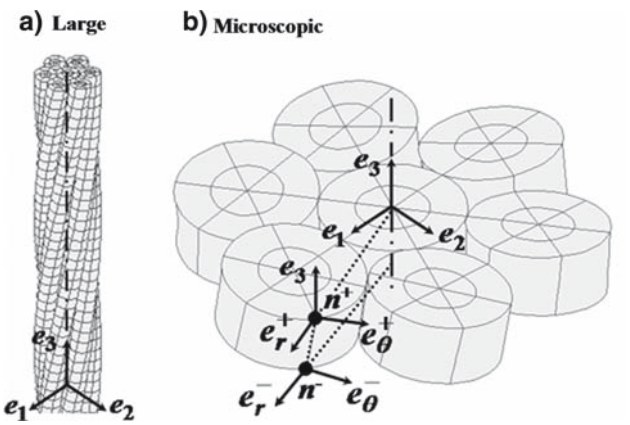

Fig. 5 FE models of the stranded cable

3.2 Single-walled carbon nanotubes

The single-walled carbon nanotubes (SWCNTs) exhibit helical symmetry [16], and the purpose of this section is to extend the applicability of the homogenization procedure to such structures.

In a first step, the geometry and mechanical modeling of the nanotube will be presented. Following the approach proposed by several authors as detailed in [18,22], the nanotubes are modeled as space-frame structures, using beams to represent atomic bonds. The reduced basic cell will then be defined, taking into account the two helical symmetries of the structure. Next the homogenization numerical implementation will be described, with a slight difference between the volumic case studied previously, since beam FE are used, with rotational DOFs. Lastly, computations are performed for SWCNTs exhibiting zigzag and armchair chiralities.

3.2.1 Nanotube modeling

The SWCNTs can be described as tubular shells of graphene sheets. They are lengthy cylinders (having spherical end-closures) with nanometer diameters and micrometer lengths.

Let us consider a plane sheet of graphene as schematized in Fig. 6. The bonds between carbon atoms form periodic hexagonal patterns [1,16,18,22,23]. A nanotube can then be viewed as a cylinder of radius R obtained by rolling up this sheet and by joining the two points O and O'. Such a SWCNT exhibits a cylindrical geometry of circumference OO' which is characterized by the two integers M and N defining its chirality (M, N) as follows (using the two basis vectors $\vec{a}_M$ and $\vec{a}_N$ depicted in Fig. 6):

$$\overrightarrow{OO}' = M \cdot \vec{a}_M + N \cdot \vec{a}_N \tag{21}$$

this vector being thus perpendicular to the SWCNT axis.

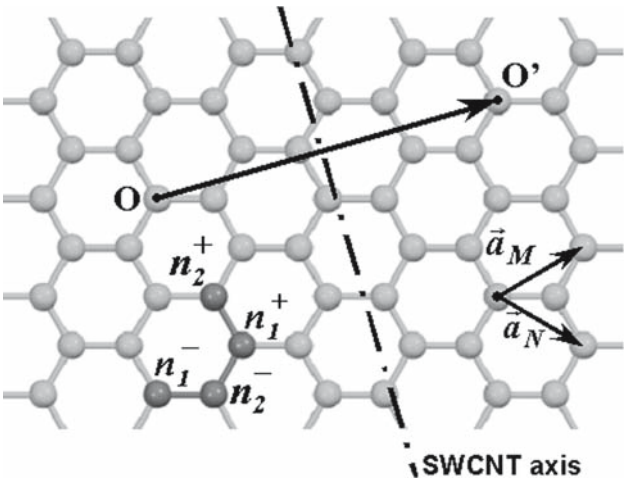

Fig. 6 Plane sheet of graphene. Definition of the geometry of a (3,1) SWCNT

Several representation examples of SWCNTs can be found in the literature, see [1,22,23] for example. Moreover, the nanotubes of (M, M) and $(M, 0)$ chirality types, are called armchair and zigzag, respectively [22,23]. The examples represented in Fig. 7a illustrate these varieties of SWCNTs.

Several approaches have been proposed for the modeling of the mechanical behavior of nanotubes, see [1,9,18] for a review. As previously performed in [18,22], the atomic interactions are modeled using Bernouilli's 3D straight linear elastic beams, the SWCNTs being then assumed to behave as space frame structures. Following the approach and results detailed in [22] obtained by linking the molecular mechanics and structural mechanics parameters, these beams are found to be 0.1421 long with a constant circular cross-section of 0.147 diameter (dimensions in nm); the longitudinal and transverse elastic moduli are $E = 5.49$ and $G = 0.871$ (values in TPa), respectively.

A SWCNT may be thus represented as a beam-like lattice structure, with a regular microstructure. The objective becomes now the description of the homogenization process in order to obtain the effective beam properties. The first step consists in the basic cell definition.

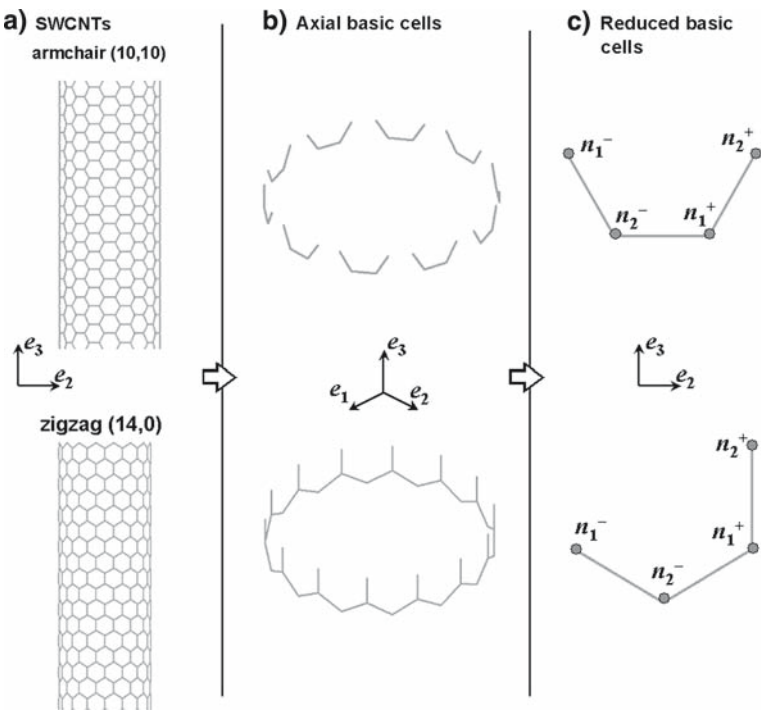

Fig. 7 Examples of large and corresponding microscopic FE models of armchair and zigzag SWCNTs

3.2.2 Reduced basic cell

In the plane of the graphene sheet, the nanotube axis is orthogonal to $\overrightarrow{OO'}$. Therefore, from the expressions of the orthogonal vectors to $\vec{a}_M$ and $\vec{a}_N$, the nanotube axis is found to be collinear to:

$$\vec{i} = (M + 2N)\vec{a}_M - (2M + N)\vec{a}_N \tag{22}$$

It is then possible to consider a SWCNT as a slender structure with axial periodicity: the associated translation vector is defined by $\vec{j} = \vec{i}/k$, where k is the highest integer which enables $\vec{j}$ to join two carbon atoms located at the same positions within hexagonal patterns. For the SWCNT ($M = 3$, $N = 1$) example depicted in Fig. 6, the axial periodicity translation is found to be $\vec{j} = 5\vec{a}_M - 7\vec{a}_N$. And for armchair and zigzag nanotubes, we obtain general forms for this translation vector representing the axial periodicity: for armchair ($M = N$), $\vec{j}$ is equal to $\vec{a}_M - \vec{a}_N$, while for zigzag SWCNTs ($N = 0$) it is $\vec{a}_M - 2\vec{a}_N$. The corresponding axial basic cell examples are shown in Fig. 7b. This axial basic cell can also be defined from the helix pitch using a chiral screw operator, as presented in [16]. From this axial basic cell, one can then apply the homogenization of periodic beam-like structures, as detailed in [4] for example. However, these basic cells are composed of a large number of hexagons, and it will be shown hereafter that taking into account the helical symmetries of the nanotube permits the definition of a helical reduced basic cell.

Indeed, a SWCNT can be viewed as a twisted structure as noticed in [1,16]. Let us come back to the plane graphene sheet shown in Fig. 6: it is easy to check that the periodic hexagonal pattern can be obtained from the repetition of an half of an hexagon, using the two translation vectors $\vec{a}_M$ and $\vec{a}_M - \vec{a}_N$. These vectors actually allows switching from the carbon atom denoted n_1^- to the carbon atom n_1^+, and also in the same way to the n_2^- and n_2^+ ones, respectively. When the graphene sheet is rolled up to form the nanotube, the straight lines generated by these two translation vectors become helices. Therefore, a SWCNT exhibits two helical symmetry properties. The reduced basic cell may be defined by a half of an hexagon, as shown in Fig. 8. Hence, comparing the reduced basic cells to the corresponding axial ones (defined from the axial periodicities as detailed previously) of the armchair and zigzag SWCNT examples depicted in Fig. 7c, it can be seen that a very important basic cell reduction is obtained.

3.2.3 Numerical implementation of the homogenization method

In Sects. 2.2 and 2.3, the three-dimensional reduced basic cell problem and its numerical FE implementation were presented. If a three-dimensional approach was used for the nanotube, the reduced basic cell shown in Fig. 9 would have been considered, with linear relationships given in Eq. (15), between the corresponding nodes of the faces ∂Y_1^- and ∂Y_1^+ on one hand, and ∂Y_2^- and ∂Y_2^+ on the other hand. As mentioned previously in Sect. 2.3, these relationships involve displacement DOFs.

Within the framework of the modeling approach described in Sect. 3.2.1, the reduced basic cell is assumed to be composed of beams. The reduced basic cell problem in that case is obtained from the three-dimensional formulation, considering that the solution of the latter problem can be approximated using Bernoulli's assumption, made on the displacement field u defined in Eq. (14), as detailed in [2,12]. In this way, the three-dimensional reduced basic cell problem depicted in Fig. 9 may be posed on a reduced basic cell constituted with beams (see Fig. 8).

In order to perform a numerical solution, this reduced basic cell is modeled using three beam FE. Due to the beam assumption, the set of linear relationships (see Eq. (15)) used initially in the three-dimensional formulation have to be modified. These relationships are now restricted to the couples of nodes $\left(n_1^-, n_1^+\right)$ and $\left(n_2^-, n_2^+\right)$ (see Fig. 8), which are located on the mean-line of the beam. In these equations, one has

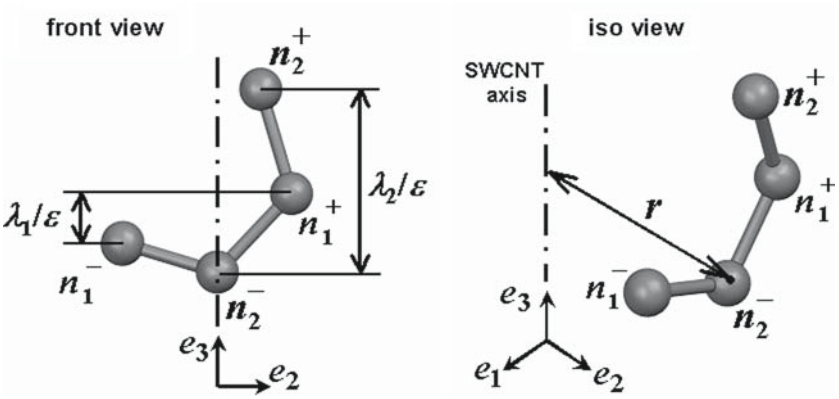

Fig. 8 General reduced basic cell of a SWCNT

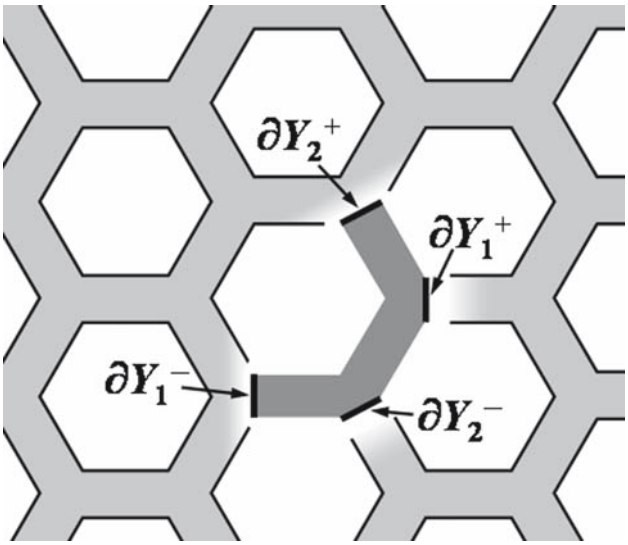

Fig. 9 Three-dimensional representation of a SWCNT reduced basic cell

$r = R/\varepsilon$ (R being the nanotube radius) and the values λ_1 and λ_2 defined in Fig. 8 have to be considered for λ. Additional relations are satisfied by the rotational DOFs. They are obtained from Eq. (15) and using Bernouilli's assumption for the bending rotations [2,12]. The relation for the axial rotation is deduced from the property that this rotation is defined as the projection of $\overrightarrow{\text{rot}}\, u/2$ on the beam axis. Denoting Θ_i^- and Θ_i^+ the rotations (expressed in the local cylindrical frames) of the opposite nodes n^- and n^+, the rotations relationships are found to be:

$$\begin{cases} \Theta_r^+ - \Theta_r^- = 0 \\ \Theta_\theta^+ - \Theta_\theta^- = 0 \\ \Theta_3^+ - \Theta_3^- = \lambda E^T/\varepsilon \end{cases} \tag{23}$$

One can check that from the Bernoulli-Navier assumption and Eqs. (15–23) on the mean-line displacements and rotations $\left(n_1^-, n_1^+\right)$, the displacements of two arbitrary corresponding points of ∂Y_1^+ and ∂Y_1^- actually satisfy Eq. (15).

It should be noticed that the exact solution of the basic cell problem is thus obtained using only three beam FE. Therefore, the overall stiffness coefficients can be computed using very concise FE models, including only four nodes and three beam elements.

3.2.4 Numerical tests

Zigzag and armchair SWCNTs are considered. It should be stressed that for such zigzag and armchair nanostructures, the coupling coefficients vanish due to the axial symmetry, i.e. $a_{ET}^{hom} = a_{TE}^{hom} = 0$. The homogenization computations are performed following the approach previously used for volume structures. Thus, two FE model types have been studied on Samcef code: first, some large length ones depicted in Fig. 7a comprising about 100 hexagonal axial periods, in order to obtain reference numerical results. Next, microscopic four nodes FE models of the reduced basic cells shown in Fig. 7c are coupled to the developed homogenization procedure using the linear relationships corresponding to Eqs. (15,23).

Table 3 Stiffness coefficients of a (14,0) zigzag SWCNT

Model	a_{EE}^{hom} (10^{-6} N)	a_{TT}^{hom} (10^{-25} N m^2)	CPU time (s)
Large FE [19]	1.208		
Present large FE	1.215	1.749	8.0
Microscopic FE	1.215	1.750	0.2

The homogenization approach has been first checked using comparisons with the results detailed in [22] obtained using a large FE model and reported in Table 3. The SWCNT studied is a zigzag one ($M = 14$, $N = 0$) represented in Fig. 7a. The stiffness coefficients of traction and torsion a_{EE}^{hom} and a_{TT}^{hom} deducted both from the Samcef large and microscopic FE models are given in Table 3. As can be seen, the homogenized results obtained from the reduced basic cell problem appear to be in very good agreement with those identified from the large ones. Moreover, as noticed previously for the spring and rope structures, the computation time reduction observed for this example is also significant as can be seen in Table 3.

Next, the study of the tensile and torsion stiffness evolutions of $(M, 0)$ zigzag and (M, M) armchair SWCNTs, for a number of circumferential hexagonal cells M varying between 5 and 40, has been performed. For each computation, the values deducted from the microscopic FE models of the reduced basic cells depicted in Fig. 7c have been compared to those obtained using the large ones: the differences are always less than 1%. The evolutions of the a_{EE}^{hom} and a_{TT}^{hom} elastic homogenized coefficients as a function of the number of circumferiental cells are plotted in Fig. 10a and b, respectively. As can be seen, the tensile stiffness evolutions appear to be proportional to the number of circumferiental cells M for both zigzag and armchair nanotubes, and the torsion coefficient evolutions follow nearly cubic dependences on M. It can be noticed that for a same number of axial hexagonal cells M, the overall stiffness coefficients of armchair SWCNT are always larger than the zigzag nanotube ones. These results, obtained immediately using the reduced basic cell FE models, demonstrate the usefulness of the homogenization procedure for the computation of SWCNTs.

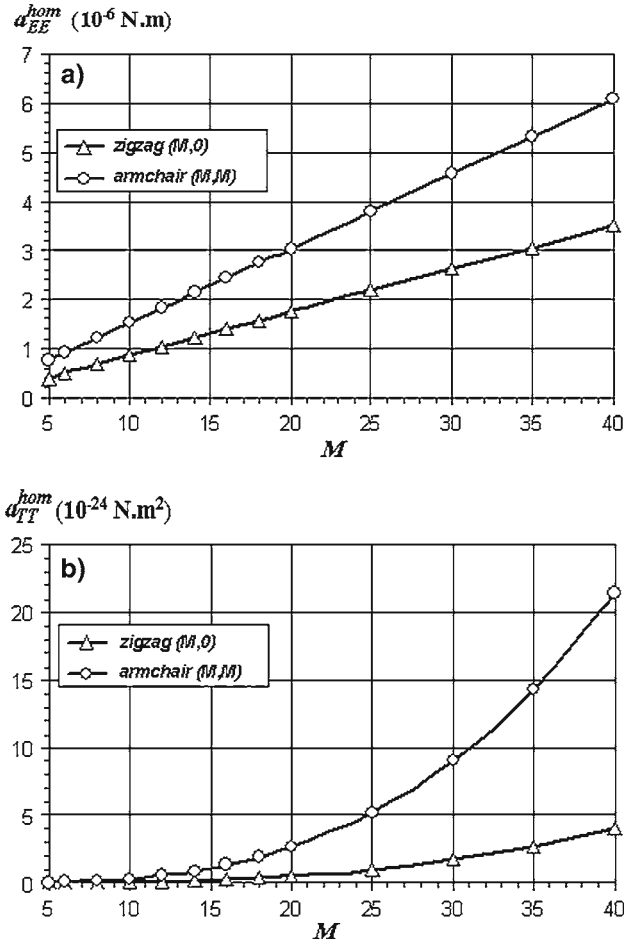

Fig. 10 Tensile and torsion stiffness evolutions of zigzag and armchair SWCNTs

4 Conclusions

Starting from the computational homogenization procedure developed for periodic axial structure, a refined approach has been developed for the computation of the overall axial stiffness of helical beam-like structures. It is shown that taking benefit of the helical symmetry, the macroscopic elastic behavior can be deducted from the solution of a microscopic problem posed on a reduced basic cell. The numerical solving can then be performed through FE computations using sets of kinematic relationships expressed in local cylindrical frames.

The efficiency and usefulness of this approach has been demonstrated foremost for volume helical structures: in this case, a reduced basic cell of arbitrary length may be considered, so the mesh used consists in only one axial layer of three-dimensional FE. Next, the computation of SWCNTs modeled as space-frame structures has been performed using a very concise model: the two helical symmetries actually enable the definition of reduced basic cells which represent only one half of a hexagon, modeled using three beam FE.

For each example treated, the stiffness homogenized values obtained showed good agreement with large length FE model results, enabling significant calculus time reductions. This allows making efficient sensitivity analysis of overall stiffness to geometrical and material parameters, as it was done for the SWCNTs. Moreover, since the size of the reduced basic cell is small, the study of localized phenomena using fine meshes can be performed, similarly to the work detailed in [11]. Work is in progress to apply this method to the study of multi-walled carbon nanotubes.

References

1. Ashrafi B, Hubert P (2006) Modeling the elastic properties of carbon nanotube array/polymer composites. Comp Sci Tech 66: 387–396
2. Buannic N, Cartraud P, L'Hostis G (1999) Homogénéisation périodique de structures ou matériaux constitués de poutres, actes du 4ème Colloque National en Calcul des Structures, Teknea pp 823–828
3. Buannic N, Cartraud P (2001) Higher-order effective modelling of periodic heterogeneous beams—part I: asymptotic expansion method. Int J Sol Struct 38:7139–7161
4. Cartraud P, Messager T (2006) Computational homogenization of periodic beam-like structures. Int J Sol Struct 43:686–696
5. Cioranescu D, Saint Jean Paulin J (1999) Homogenization of reticulated structures. Appl Math Sci, Springer, New York
6. Costello GA (1997) Theory of wire-rope, 2nd edn. Springer, Berlin
7. Ding X, Selig JM (2004) On the compliance of coiled springs. Int J Mech Sci 46:703–727
8. Ghoreishi SR, Messager T, Cartraud P, Davies P (2006) Validity and limitations of linear analytical models for steel wire strands under axial loading, using a 3D FE model. Int J Mech Sci (submitted)
9. Guo X, Wang JB, Zhang HW (2006) Mechanical properties of single-walled carbon nanotubes based on higher order Cauchy–Born rule. Int J Sol Struct 43:1276–1290
10. Jiang WG, Yao MS, Walton JM (1999) A concise finite element model for simple straight wire rope strand. Int J Mech Sci 41: 143–161
11. Jiang WG, Henshall JL (2000) A novel element model for helical springs. FE Anal Des 35:363–377
12. Kalamkarov AL, Kolpakov AG (1997) Analysis, design and optimization of composite structures. Wiley, Chichester
13. Kolpakov AG (1991) Calculation of the characteristics of thin elastic rods with a periodic structure. J Appl Math Mech 55:358–365
14. Kolpakov AG (2004) Stressed composite structures: homogenized models for thin-walled non-homogeneous structures with initial stresses. Springer, Berlin
15. Labrosse M (1998) Contribution à l'étude du rôle du frottement sur le comportement et la durèe de vie des câbles monocouches. PhD Thesis, University of Nantes
16. Mintmire JW, White CT (1995) Electronic and structural properties of carbon nanotubes. Carbon 33:893–902
17. Nawrocki A, Labrosse M (2000) A finite element model for simple straight wire rope strands. Comp Struct 77:345–359
18. Qian D, Wagner GJ, Liu WK, Yu MF, Ruoff RS (2002) Mechanics of carbon nanotubes. Appl Mech Rev 55:495–533
19. Roshan Fekr M, McClure G, Farzaneh M (1999) Application of Adina to stress analysis of an optical ground wire. Comp Struct 72:301–316

20. Slepyan LI, Krylov VI, Parnes R (2000) Helical inclusion in an elastic matrix. J Mech Phys Sol 48:827–865
21. Stephen NG, Zhang Y (2006) Eigenanalysis and continuum modeling of pre-twisted repetitive beam-like structures. Int J Sol Struct 43:3832–3855
22. Tserpes KI, Papanikos P (2005) Finite element modeling of single-walled carbon nanotubes. Comp Part B 36:468–477
23. Zhang CL, Shen HS (2006) Buckling and postbuckling analysis of single-walled carbon nanotubes in thermal environments via molecular dynamics simulation. Carbon 44:2608–2616